High operating temperature HgCdTe coupled cavity plasmonic infrared photodetectors

(Article begins on next page)

09 November 2024

High operating temperature HgCdTe coupled cavity plasmonic infrared photodetectors

M. VALLONE,[1,*] ID M. GOANO,[1,2] ID AND A. TIBALDI[1] ID

[1]*Dipartimento di Elettronica e Telecomunicazioni, Politecnico di Torino, corso Duca degli Abruzzi 24, 10129 Torino, Italy*
[2]*IEIIT-CNR, corso Duca degli Abruzzi 24, 10129 Torino, Italy*
*marco.vallone@polito.it

Abstract: Increasing the operating temperature while enhancing detectivity is paramount for the advancement of HgCdTe infrared detectors. In this context, the integration of plasmonic nanostructures emerges as one of the most intriguing avenues, promising breakthroughs in infrared sensing capabilities. Multiphysics TCAD simulations of *pin* nanostructured focal plane photodetector arrays unveil the potential benefits of submicron absorber thicknesses, that promise detectivities more than twice as large as those provided by conventional 5 μm-thick absorbers, besides enabling operating temperatures up to 260 K. Such performance increase is discussed through the combination of numerical simulations and quantum mechanical treatment based on the occupation number formalism, describing the interaction between plasmonic and optical cavity modes responsible for the spectral broadening of the optical response, allowing for good coverage of the entire mid-infrared band ($\lambda \in [3,5]\,\mu$m).

1. Introduction

High operating temperature (HOT) infrared (IR) photodetectors [1–3] are presently obtained with nBn or pBn barrier detectors [4–11] or adopting fully-depleted double-layer planar heterostructures (DLPH) [12–17]. Although successful in principle, these strategies exhibit some realization problems. DLPH detectors require extremely low residual doping in the absorber [13,14,16]. Concerning instead barrier detectors, composition and doping profiles [9,18,19], as well as the annealing time during fabrication [7], need to be carefully calibrated to avoid negative effects on the dark current. Moreover, the valence band barrier must be reduced to favor the flow and collection of the photogenerated minority carriers. To this end, superlattice-based barriers [11,18,20] or pBn profiles with acceptor doped barriers are often considered, and in the latter case, a n^+p^+ tunnel-junction is often required [19] to improve the electrical p-contact, increasing fabrication complexity.

In this view, trying to increase the operating temperature and simplify the critical cryocooler block requires investigating new frontiers. The community is investing increasing efforts to improve the responsivity [21] of focal plane array (FPA) detectors by favoring the coupling of light to the absorbing material through nanostructured surfaces [22,23] or plasmonic structures [24–32]. Surface plasmon polaritons (SPPs) have interesting characteristics, and in principle could be utilized for this purpose. SPPs are electromagnetic modes that can propagate at metallic-dielectric interfaces, where collective surface excitations of free electrons are coupled to evanescent electromagnetic fields in the dielectric [33,34].

At present, even considering problems such as their toxicity, mercury cadmium telluride ($Hg_{1-x}Cd_xTe$, MCT) alloys are among the leading electro-optic materials used for IR optical sensors, still after 65 years since their discovery and first application [35–38]. One of the main figures of merit quantifying the performance of IR photodetectors is the specific detectivity D^*

[5]

$$D^* \approx \frac{S^{1/2}\mathcal{R}}{\sqrt{2\,e\,I_\text{dark}}}, \tag{1}$$

where e is the elementary charge and S is the illuminated area of the detector. As a general rule, D^* is proportional to the ratio between $\mathcal{R}$ and the root mean square (rms) of the noise current [21, Ch. 2]. Strictly speaking, Eq. (1) accounts for the shot noise contribution only. In MCT photodetectors, there is a variety of noise sources (mainly Johnson, shot and $1/f$ noise [21, Ch. 3 and Ch. 9, 39,40]). The physical mechanism behind $1/f$ noise has not been clearly identified. Yet, there is a general consensus about its relation with defects in the semiconductor, to some extent related to the dynamics of Shockley-Read-Hall generation/recombination processes. Similarly, shot noise is strictly related to $\sqrt{I_\text{dark}}$. On the other hand, diffusion noise sources are mainly related to temperature and to the local carrier density [41, eq. (1.63)]. In this view, contrary to shot (and probably $1/f$) noise, diffusion noise can be hardly mitigated modifying geometrical device parameters such as absorber thickness. Yet, considering that most of the device is depleted (apart from quasi-neutral regions), in this work we consider it negligible.

Equation (1) emphasizes the importance of the MCT absorber thickness t_abs as the main geometrical design parameter. In fact, if a larger t_abs improves the responsivity $\mathcal{R}$ by favoring the absorbance, on the other hand it increases also the dark current I_dark, which is proportional to the detector volume – hence, to t_abs – and limits the high-temperature operation of the detector. As a reminder, $\mathcal{R}$ is defined as

$$\mathcal{R} = \frac{J_\text{ph}}{P}, \tag{2}$$

where P is the optical power density and $J_\text{ph} = J - J_\text{dark}$ is the photocurrent density, where J and J_dark are the current density under illumination and in dark, respectively.

Aiming to overcome the trade-off between responsivity and dark current towards high operating temperature (HOT) detectors [1–3], it is possible to employ SPPs to enable a reduction of t_abs (therefore, of the dark current) without introducing any significant penalty on the responsivity and enhancing the detectivity by an increase of the absorbed photon density for given P.

SPPs can be excited by plasmonic periodic structures, where metal nanoparticles fabricated on the illuminated face of a detector generate a localized surface plasmon resonance (LSPR) [33]. When arranged in two-dimensional (2D) lattices, stronger resonances arise from the interaction between the light diffracted by the lattice and the LSPR modes. These are Fano-type resonances called surface lattice resonances (SLRs) and their wavelength $\lambda_{p,q}$ is determined by the lattice period Λ (here p, q are integers) [42–44].

If the array of nanoparticles is part of an optical array-absorber-reflector resonator similar to Fig. 1 whose details will be fully described further in the present work, the reflector can compensate for the damping of the SLRs and excite SPP modes for discrete values of wavelength $\lambda_{p,q}$, which eventually interact with the optical cavity (OC) modes [42,44–46].

Several applications have been developed so far to exploit SPPs in optoelectronic devices: most of them are THz and IR detectors in the long wavelength (LWIR) and very-long-wave infrared (VLWIR) band ($\lambda \in [8, 12]\,\mu m$ and $\lambda > 12\,\mu m$, respectively) exploiting type-II superlattices (T2SL) [47] or intersubband transitions in quantum-well infrared photodiodes (QWIP) [48–51], plasmonic-organic-hybrid electro-optic modulators [52–54], or plasmonic cavities integrating graphene (for a review see, e.g., [55] and references therein). Other applications are aimed at reducing the inhomogeneous broadening of the material gain in quantum cascade lasers [56], or at developing solar cells with quasi-ideal absorption efficiency [57].

Several plasmonic solutions have been proposed for IR detectors in the MWIR band (mid-wavelength IR, $\lambda \in [3, 5]\,\mu m$, see a review in [43]). However, only very recent contributions include MCT as absorber in IR plasmonic detectors, although for temperature close to liquid nitrogen [58], or at room temperature but without simulating or measuring electro-optical
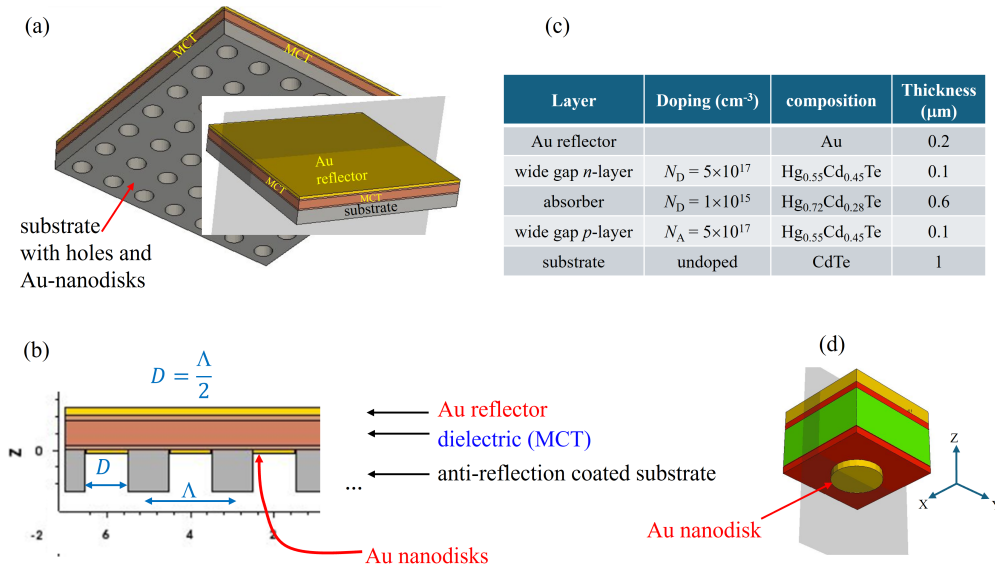
Layer	Doping (cm⁻³)	composition	Thickness (µm)
Au reflector		Au	0.2
wide gap *n*-layer	$N_D = 5\times10^{17}$	Hg$_{0.55}$Cd$_{0.45}$Te	0.1
absorber	$N_D = 1\times10^{15}$	Hg$_{0.72}$Cd$_{0.28}$Te	0.6
wide gap *p*-layer	$N_A = 5\times10^{17}$	Hg$_{0.55}$Cd$_{0.45}$Te	0.1
substrate	undoped	CdTe	1

Fig. 1. (a) The plasmonic cavity with (b) its 2D section, showing a 2D Λ-periodic nanoarray of holes and Au nanodisks. In the table (c), the detail of the epitaxial layers, and in (d) the elementary cell needed for simulations, where periodic boundary conditions are imposed on the $\hat{x}$, $\hat{y}$ directions.

properties like $\mathcal{R}$ or D^* [59]. Concerning modeling, most of the literature does not include three-dimensional multiphysics simulations (i.e., full-wave electromagnetic, followed by electrical transport), except for recent examples [43,60].

In 2007 Teledyne proposed the "Rule 07" [61] as the fundamental metric for predicting the dark current in Hg$_{1-x}$Cd$_x$Te IR detectors. The Rule was reviewed in 2019 by proposing the "Law 19", specifically for fully-depleted absorbers [16], which demonstrated very low values for dark current – and consequently high D^* – in HOT detectors, as long as Hg$_{1-x}$Cd$_x$Te is grown with ultra-low residual doping and defect density (in the order of 10^{13} cm^{-3}), a very challenging task whose achievement could be a major issue.

In the present work, SPPs are presented as a key building block to reduce dark current and to obtain enhanced detectivity D^* close to room-temperature, which could be an alternative approach, not considered so far, in case very low values of residual doping are not technologically-achievable. Moreover, the SPP-OC mode interaction is exploited to achieve a broadening of the detectivity spectrum, which increases the optical bandwidth of the photodetector. The paper is structured as follows. After providing in Section 2 an overview of the adopted computational methods and material parameters, Section 3 describes the excitation of plasmonic modes, their role in the enhancement of D^* [48–50,58,59] and, in a more detailed way, the mechanism of the SPP-OC interaction, modeled through a quantum mechanical treatment based on the occupation number formalism. Relying on these foundations, in Section 4 we provide combined electromagnetic and transport simulations of the single pixel shown in Fig. 1, where the MCT absorber is a HgCdTe-based heterostructure with *pin* doping profile. In the end, Section 5 summarizes the main outcomes.

2. Description of the simulation framework

The three-dimensional (3D) multiphysics model we developed [54,62–65] integrates the Synopsys RSoft FullWAVE tool [66], solving the electromagnetic problem with a finite-difference time-domain (FDTD) approach [67,68], and the Synopsys TCAD Sentaurus [69], which addresses the carrier transport problem in the drift-diffusion approximation. The simulation workflow starts from the FDTD simulation of the detector, assuming a fine discretization ($\approx \lambda/30$) and a monochromatic plane-wave illumination, whose electric field exhibits the time-harmonic form $\mathbf{E} = E_0 \exp(\mathbf{kr} - \omega t)$ and is oriented along the $\hat{x}$ direction. All the detector variants described throughout the present work have their illuminated face in the (x, y) plane. We consider normal incidence (incidence angle $\theta = 0$). The incident electric field amplitude is specified in terms of the input power density P. As a result, the FDTD solver provides the spatially-resolved electromagnetic field, from which it is possible to evaluate the absorbed photon density A_{opt} as

$$A_{\text{opt}}(\lambda, r) = -\frac{\vec{\nabla} \cdot \langle \vec{S}(\lambda) \rangle}{h\text{c}/\lambda}, \tag{3}$$

i.e., as the divergence of the time-averaged Poynting vector $\vec{S}$ [70, Sec. 6.8] [63,64,71–74]. Here h and c are the Planck constant and the light velocity in vacuum. It is to be remarked that RSoft includes realistic models of the complex refractive index of the material alloys under investigation, taking into account wavelength and temperature dependencies. In particular, ϵ_{Au} and ϵ_{MCT} indicate the relative complex dielectric functions of gold and MCT, respectively. For ϵ_{MCT} we adopted the model described in [75] and [76, Sec. 9.6]. Regarding ϵ_{Au}, we adopted the Drude form in [77],

$$\epsilon_{\text{Au}}(\omega) = \epsilon_\infty - \frac{\omega_p^2}{\omega^2 - i\omega\omega_t}, \tag{4}$$

where $\epsilon_\infty = 1$, $\omega_p = 1.37 \times 10^{16}$ rad/s, and $\omega_t = 4.65 \times 10^{13}$ rad/s.

By imposing periodic boundary conditions (PBCs) along $\hat{x}$ and $\hat{y}$, and convolutional perfectly matched layer (CPML) absorbing BC [78] along $\hat{z}$, we took advantage of the Λ-periodicity of the structure shown in Fig. 1 to simulate just an elementary cell (panel (d)), obtaining results which are representative of an entire pixel [43] with much lower computational effort.

The modeling of the electromagnetic response can be followed by carrier transport simulations to assess J_{dark} and, under illumination, J_{ph}, $\mathcal{R}$ and D^*. To this end, the employed commercial simulation suite [69] performs a discretization on a 3D domain of the Poisson-drift-diffusion system [64,79] using a stabilized finite-box method, allowing for great flexibility in the definition of material parameters and in the computational grid optimization, enabling local refinements for critical regions (such as junctions between different materials and/or doping concentrations) [69]. The adopted model employs the rate of photogenerated carriers, evaluated from A_{opt}, as a source term in the continuity equations. Fermi-Dirac statistics are used for the carrier density, as described in [64], where all the details about the mole fraction and temperature dependent MCT parameters are also reported (see also Table S1 in Supplement 1). The electrostatic model takes into account the incomplete ionization of the doping densities. The carrier transport model includes the Shockley-Read-Hall (SRH) and Auger generation-recombination (GR) processes, modeled as in [80] and [81], respectively.

3. Plasmonic resonances: starting from a simpler structure

This section is focused only on the electromagnetic problem, and all the simulations have been performed at $T = 160$ K. The most interesting computed figures of merit returned by the

simulation are the spectral absorption efficiency

$$\eta = \frac{hc}{\lambda P} \int_V A_{\text{opt}} \, d^3\mathbf{r} \tag{5}$$

and the spatial distribution of A_{opt}, obtained from the electric and magnetic field components (V is the absorber volume, and $\mathbf{r}$ is the position vector).

The single pixel shown in Fig. 1 consists of a CdTe substrate on which a HgCdTe-based heterostructure is epitaxially grown with the doping and composition profiles detailed in the table reported in panel (c), followed by a 0.2 μm-thick Au reflector. Concerning the fabrication, appropriate lithographic and etching techniques (e.g., electron-beam lithography) can be employed to obtain a Λ-periodic series of nanoholes on the substrate, where, by sputtering, 50 nm-thick gold nanodisks with diameter $D = \Lambda/2$ can be deposited on their bottom (see a discussion concerning this choice for D in [43, Fig. 3(a)]). When the detector is illuminated from below, several possible optical and plasmonic modes can be involved, as anticipated in short in Section 1.

It is to be remarked that the scope of the present investigation is to demonstrate the potential benefit of plasmonics to enhance performance of MCT-based MWIR detectors, as an alternative to reach record-level of residual doping. The details of the manufacturing process for such devices is beyond the scope of this work.

Aiming to provide an effective description of the physics ruling the absorber operation, this section is structured as follows. First, we perform a preliminary investigation of the dispersion characteristics of the simplified Au-MCT-air slab cavity sketched in Fig. 2(a). Then, the full structure, including the nanodisks array, is studied and its operation is interpreted in the light of the slab cavity.
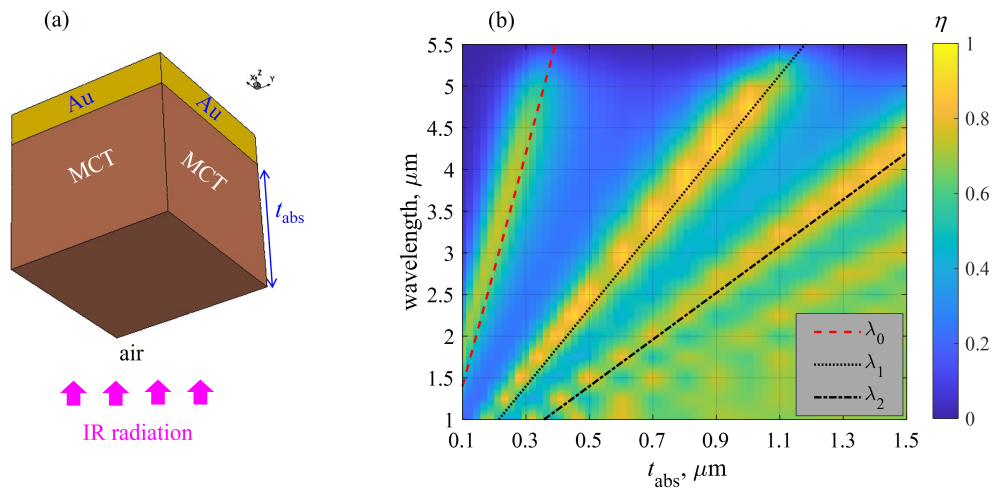

Fig. 2. (a) The metal-dielectric-air optical cavity. (b) Color map of the spectral absorption efficiency as function of t_{abs}. The lines marked with $\lambda_{0,..2}$ have been plotted according to Eq. (6).

3.1. Dielectric-metal slab cavity

This section presents a study of the absorption features of the slab cavity sketched in Fig. 2(a). Here, the dielectric is a t_{abs}-thick absorber with the same composition of the absorber described in the table reported in Fig. 1(c), whose cutoff wavelength is around 5.38 μm at $T = 160$ K, hence suitable to operate in the MWIR band.

Figure 2(b) shows a color map of the spectral absorption efficiency η as function of t_{abs}, obtained with a series of FDTD electromagnetic simulations assuming normal-incidence plane-wave excitation, after having appropriately discretized the (t_{abs}, λ) parameter space. It can be seen at a glance that the map exhibits three high-absorption stripes. These regions are related with the resonances of the optical cavity. Indeed, it is known that the round-trip phase-shift condition for an optical cavity, for which reflectivity is minimum, reads [82]

$$n_{MCT} t_{abs} = \left(m + \frac{1}{2} \right) \frac{\lambda_m}{2}, \quad m = 0, 1, \ldots \quad (6)$$

Remarkably, the lines $\lambda_{0\ldots2}$, indicating the loci obtained solving Eq. (6) for $m = 0 \cdots 2$, match perfectly with the high-absorption stripes. However, we should remark that an anti-reflection coating is usually deposited on the illuminated face, which substantially quenches the optical resonances (i.e., the OC modes) and leaves only a simple double-pass effect ensuing from the Au-reflector.

3.2. Coupling OC and SPP modes

While the example reported in the previous section is very useful to relate high-absorption regions with resonance properties of the detector, it does not feature any signature from SPPs. Indeed, SPPs are surface collective excitations of free electrons that can propagate along a metal-dielectric interface, satisfying the dispersion relation

$$k_x = \frac{2\pi}{\lambda} \left(\frac{\epsilon_{Au} \epsilon_{MCT}}{\epsilon_{Au} + \epsilon_{MCT}} \right)^{1/2} \quad (7)$$

which implicitly indicates that the SPP is propagating along $\hat{x}$. Yet, with a slab waveguide, it is not possible to excite a SPP mode, as the boundary conditions of Maxwell's equation for planar stratified normal-incidence problems enforce the continuity of the transverse wavevector components, i.e., $k_x = 0$.

In order to excite SPP modes, it is necessary to introduce optical scattering mechanisms. A fundamental idea could be to introduce an isolated nanoparticle, e.g., a single Au disk, which could scatter the incident plane wave in all the directions. This mechanism is rather ineffective, since only a fraction of the radiation would be coupled to the SPP [42,44]. In this view, it is possible to engineer diffraction by using a periodic lattice of nanoparticles, rather than a single one. In fact, this allows to diffract for [28–30]

$$\mathbf{K}_{p,q} = \frac{2\pi}{\Lambda} \left(\sin(\theta) \, \hat{u} \pm p \, \hat{x} \pm q \, \hat{y} \right), \quad p, q = 0, 1, \ldots \quad (8)$$

where $\hat{u}$ is a unit vector in the direction of the in-plane component of the incident light wavevector $\mathbf{k}$, and we assumed that the reciprocal lattice vectors are parallel to the unit vectors $\hat{x}$ and $\hat{y}$. This allows the light diffracted by the array to interact with the localized plasmons associated with the nanoparticles, i.e., the LSPRs, obtaining a Fano-type SLR [42–44]. However, aiming to obtain a strong SPP mode rather than a SLR, it is necessary to design the lattice period Λ in such a way that the wavevector plane wave diffracted by the nanostructure carrying the majority of the power (often, the first diffracted order) matches the SPP k_x. Based on this idea, by equating k_x in Eq. (7) to $\left| \mathbf{K}_{p,q} \right|$ for normal incidence, we obtain the condition

$$\lambda_{p,q} = \frac{\Lambda}{\sqrt{p^2 + q^2}} n_{eff} \quad (9)$$

$$n_{eff} = \mathfrak{R} \sqrt{\frac{\epsilon_{Au} \epsilon_{MCT}}{\epsilon_{Au} + \epsilon_{MCT}}}. \quad (10)$$

This corresponds to the wavelength of the impinging plane wave that excites the SPP modes ($\mathfrak{R}$ indicates the real part. It is to be further remarked that the dielectric functions ϵ_{Au} and ϵ_{MCT} also

depend from wavelength). For further reference, we define the first order plasmonic resonance with the special symbol $\lambda_{\text{SPP}} = \lambda_{0,1} = \lambda_{1,0}$. The negative and quite high value of $\mathfrak{R}(\epsilon_{\text{Au}})$ in the MWIR implies a non-optimal confinement of the plasmonic mode on a subwavelength volume, and the use of a material other than gold will be investigated in a future work. Nevertheless, the present choice offers more numerical stability for the simulations and it constitutes a "worst case", sufficient to describe the potential benefit of a plasmonic cavity.

As a first modeling approach, we focused on the elementary cell shown in Fig. 3(a), imposing PBCs along $\hat{x}$ and $\hat{y}$, and CPML along $\hat{z}$, choosing $\Lambda = 1$ μm and $D = \Lambda/2$. The result obtained by performing the same FDTD electromagnetic simulations as in Section 3.1 is shown in Fig. 3(b) as color map in the $(t_{\text{abs}}, \lambda)$ parameter space. Compared to the OC results in Fig. 2(b), here we can notice that the optical modes are perturbed and interrupted by the crossing of the SPP mode, which is excited at wavelength λ_{SPP} (solid black line). For n_{eff}, we adopted the real part of the Helmholtz eigenvalue for a metal-dielectric-metal cavity with thickness t_{abs} [83]. It is very close to the value provided by Eq. (10), but this way also describes the small λ_{SPP} change induced by t_{abs}, plotted in Fig. 2(b) according to Eq. (9).
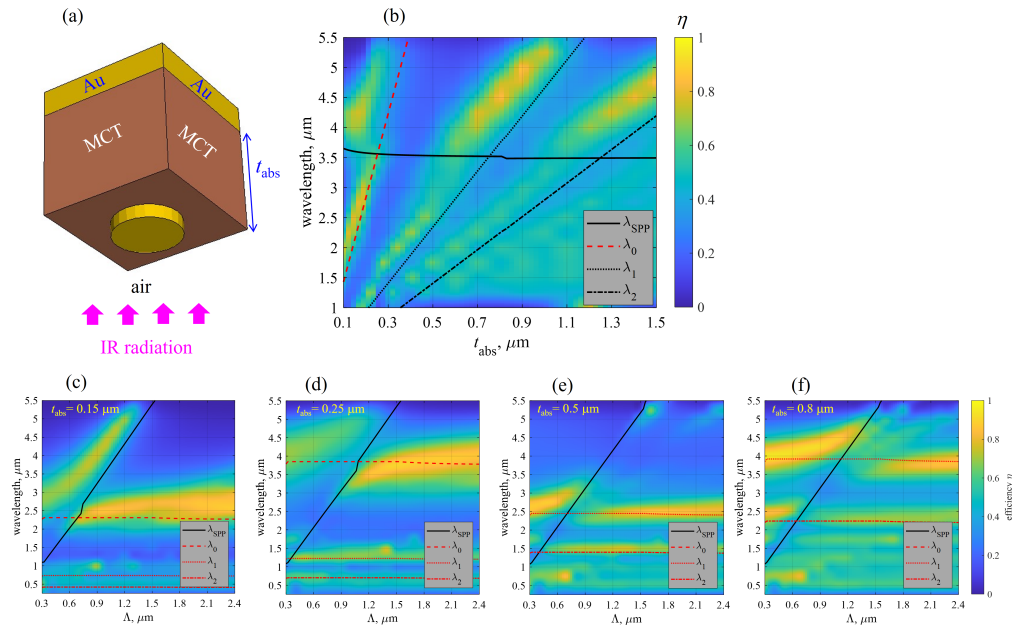

Fig. 3. (a) The elementary cell for the study of hybridized plasmonic cavity resonances, representative of a pixel indefinitely extended in the XY plane. (b) Color map of η for $\Lambda = 1$ μm, in the $(t_{\text{abs}}, \lambda)$ parameter space. Color map of η for $t_{\text{abs}} = 0.15$ μm (c), 0.25 μm (d), 0.5 μm (e), 0.8 μm (f), in the (Λ, λ) parameter space.

Deeper physical insight can be provided by a different approach, which consists of performing a campaign of electromagnetic FDTD simulations on a different parameter space, i.e., (Λ, λ), for a given value of t_{abs}. These results are shown in Fig. 3(c)-(f) for $t_{\text{abs}} = 0.15, 0.25, 0.5, 0.8$ μm, respectively. In this representation, the optical modes λ_m are horizontal lines and have been plotted according to Eq. (6), while the plasmonic mode λ_{SPP} is the diagonal black solid line, which also in this case has been plotted according to Eq. (9). We can notice several interesting facts. First, as expected, the values of the optical modes λ_m increase rapidly with t_{abs}, and λ_0 falls out of parameter space in panels (e) and (f). Second, there is a clear anti-crossing behavior between the optical and plasmonic modes. Third, the SPP mode λ_{SPP} does not correspond to

high η as probably expected, but it makes optical modes to bend when approaching it. All this deserves an in-depth investigation, which will be pursued in Section 3.3.

3.3. Hybridized optical and plasmonic modes

Section 3.2 aimed at studying coupling power in the SPP mode by equating the SLR and the SPP dispersion relations, i.e., $\left|\mathbf{K}_{p,q}\right|$ and k_x, respectively. The next step is to notice that the anti-crossing behavior observed in Fig. 3 can be interpreted as a synchronization condition between two uncoupled worlds, namely, the OC modes and the SPP modes. A more realistic approach is based on describing the two worlds as a one. In particular, the interaction between the optical cavity (OC) and the plasma oscillation modes (SPP) can be described on the basis of several different formalisms, which reveal to be equivalent at low coupling. One could start from Maxwell's equations, defining a polarization current which describes the coupling between OC and SPP modes, and setting up a coupled-mode theory (CMT) formulation [84]. Meanwhile, the formulation developed in this work is based on the occupation number formalism. In particular, by considering the full system Hamiltonian

$$\hat{H} = \hat{H}_{\mathrm{OC}} + \hat{H}_{\mathrm{SPP}} + \hat{H}_{\mathrm{int}}, \tag{11}$$

where $\hat{H}_{\mathrm{OC}}$ and $\hat{H}_{\mathrm{SPP}}$ describe the free OC and SPP modes, respectively, and $\hat{H}_{\mathrm{int}}$ is the SPP-OC interaction Hamiltonian, we can develop our model in the occupation number formalism [85,86]. If we consider only one OC and one SPP mode interacting under the hypothesis of low optical power density and weak coupling, as it is the case with current IR detectors, $\hat{H}$ is

$$\begin{aligned}
\hat{H} &= E_{\mathrm{OC}}\, \hat{a}^\dagger \hat{a} + E_{\mathrm{SPP}}\, \hat{b}^\dagger \hat{b} + \mathrm{i}\gamma \left(\hat{a}^\dagger - \hat{a}\right)\left(\hat{b}^\dagger + \hat{b}\right) + \delta \left(\hat{b}^\dagger + \hat{b}\right)^2 \\
\gamma &= I_0 \frac{\hbar \Omega_{\mathrm{pl}}}{2} \sqrt{\frac{E_{\mathrm{OC}}}{E_{\mathrm{SPP}}}} \\
\delta &= K_0 \frac{\left(\hbar \Omega_{\mathrm{pl}}\right)^2}{E_{\mathrm{SPP}}},
\end{aligned} \tag{12}$$

which is consistent with similar formulations (see, e.g., [87–91]), and whose derivation has been described in detail in Supplement 1. Here, E_{OC} and E_{SPP} are the OC and SPP energies corresponding to λ_m (for given m) and λ_{SPP} provided by Eq. (6) and Eq. (9), respectively. Furthermore, $\hat{a}^\dagger$ ($\hat{a}$) are the bosonic operators for the creation (destruction) of photons and $\hat{b}^\dagger$ ($\hat{b}$) are similar operators for plasmons. γ is the SPP-OC interaction energy and it is proportional to the plasma frequency Ω_{pl} and to I_0, the superposition integral between the interacting SPP and OC modes ($\hbar$ is the reduced Planck constant), δ is the SPP-SPP dipole-dipole interaction energy, and K_0 is a plasmon-plasmon coupling constant, set to unity throughout this work (when fitting experimental data, K_0 and I_0 should be treated ad fitting parameters).

$\hat{H}$ is similar to the Hopfield-Dicke Hamiltonian [92,93] and can be diagonalized by a standard method as described in Supplement 1, which returns the eigenvalues as

$$E_\pm^2 = \frac{E_{\mathrm{OC}}^2 + E_{\mathrm{SPP}}^2 + 2E_{\mathrm{SPP}}\delta}{2} \pm \frac{1}{2}\sqrt{\left[E_{\mathrm{OC}}^2 - \left(E_{\mathrm{SPP}}^2 + 2E_{\mathrm{SPP}}\delta\right)\right]^2 + 16\gamma^2 E_{\mathrm{SPP}} E_{\mathrm{OC}}}, \tag{13}$$

often indicated in the literature as the "upper" (E_+) and "lower" (E_-) SPP-OC hybrid modes. The mode splitting at the SPP-OC crossing is given by

$$\Delta = (E_+ - E_-)\big|_{E_{\mathrm{SPP}}=E_{\mathrm{OC}}} \approx 2\gamma\big|_{E_{\mathrm{SPP}}=E_{\mathrm{OC}}} = I_0\, \hbar \Omega_{\mathrm{pl}}, \tag{14}$$

where the validity of the approximate equality is discussed in Supplement 1.

In Fig. 4(a),(b) we show two examples for the calculation of η as color maps in (Λ, λ) parameter space, where we have also superimposed the curves for $E_{\pm}$, having treated I_0 as fitting parameter. If t_{abs} is increased, the superposition integral between the SPP and OC modes decreases, since most of the SPP near field is close to the reflector. This leads to a decrease in Δ, which can be observed in Fig. 4(c).
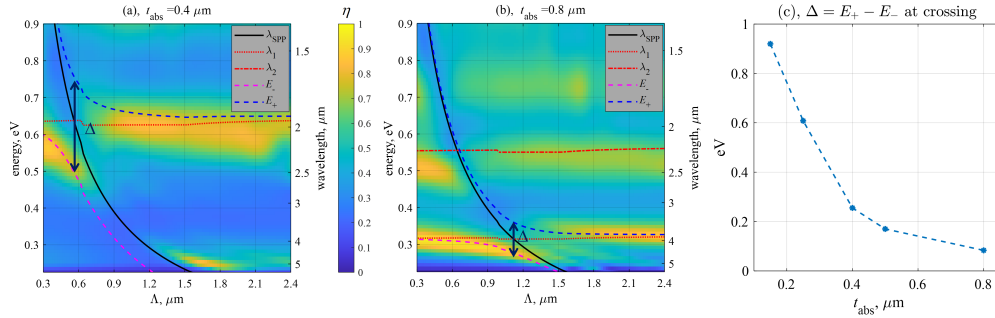

Fig. 4. Color maps of η for $t_{abs} = 0.4$ μm (a) and 0.8 μm (b), on the (Λ, E) parameter space ($E = 1.24/\lambda$, where E is in eV and λ in micrometers), where the lines E_+ and E_- are also shown. (c) The modes separation energy Δ for the $\lambda_{m=1}$ OC mode, as function of t_{abs}, as estimated from the color maps.

A considered hybrid mode can have a predominantly optical or plasmonic character depending on the considered point (Λ, λ), as shown in Fig. 5. The character of the resonance is predominantly optical if the point under consideration is closer to the OC mode λ_m. In this case, most of the absorption takes place in the bulk of the absorber, as shown in Fig. 5(b). Conversely, the resonance is predominantly plasmonic if the point under consideration is closer to λ_{SPP} and absorption takes mostly place close to the nanodisks, as in Fig. 5(d).
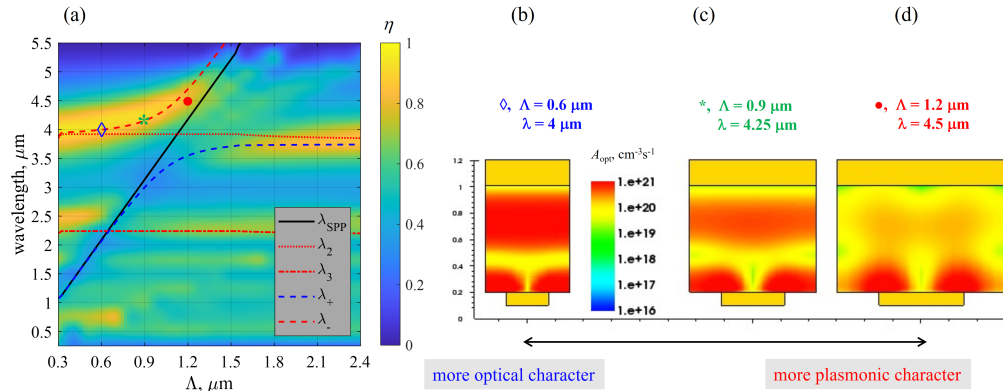

Fig. 5. (a) Color map of η for $t_{abs} = 0.8$ μm on the (Λ, λ) parameter space, with the lines $\lambda_{\pm} = 1.24/E_{\pm}$ (where E is in eV and λ in micrometers). (b)-(d) Distribution of A_{opt} for three couples of (Λ, λ) along the "lower" mode.

The good agreement between the stripes with high absorption in the color maps of η (Fig. 4 and Fig. 5) and the $E_{\pm}$ given by Eq. (13) is worth noting. Although the former is a result from classical electromagnetism, while the latter ($E_{\pm}$) comes from a quantum electrodynamics approach, they still agree well. The reason for this lies in the low-coupling regime. Actually, if we followed the CMT to describe the SPP-OC coupling (i.e., remaining in classical electromagnetism), we would get different $E_{\pm}$ (see, e.g., [94] and Supplement 1 for the explicit expressions and a brief

discussion), but the two sets of curves would be very similar. The two sets of $E_\pm$ give significantly different results only in the strong-coupling regime ($\delta \neq 0$, $\gamma \approx E_{OC}$), a situation that is far from the present case, but characterized by a growing interest, e.g., for the development of polaritonic quantum-cascade detectors [50], light-emitting diodes based on intersubband polaritons [95], and in general in quantum devices based on collective light-matter coupled states [96,97].

4. Combined electromagnetic and transport simulations

Section 3 is mainly focused on the optical features of the photodetector. Aiming to evaluate, through a comparative appraisal, the advantages of plasmonic MCT detectors versus standard devices, this section is dedicated to the multiphysics simulation at $T = 160\,\text{K}$ and $260\,\text{K}$ of the MCT-based heterostructure shown in Fig. 1, where all parameters of the epitaxial layers are given in the table in the figure.

It is to be remarked that the dark current is a figure of merit of major importance for IR detectors. This is mainly originated by the GR processes mentioned in Section 2. In this view, aiming to understand the importance of considering thin absorbers as building blocks towards high operating temperatures, some remarks are in order.

The SRH lifetime τ_{SRH} is only related to the material defect density and carrier trapping cross sections [80], and thus it may be considered a technology-dependent parameter, not associated with any fundamental physical process. We use for τ_{SRH} a value of $10\,\mu\text{s}$, which is representative of medium-quality materials [14,18]. Auger lifetime τ_{Aug} is not related to the material quality, as it depends only on the MCT Cd mole fraction, the temperature and doping density. In particular, τ_{Aug} decreases rapidly for increasing temperature, corresponding to a steep increase of J_{dark}. Since J_{dark} depends mainly on lifetimes τ_{SRH} and τ_{Aug} and from the absorber thickness t_{abs} (see, e.g., [10,18,39] for an extended discussion about this point), the opportunity to reduce t_{abs} without penalizing $\mathcal{R}$ could make thin, plasmonic MCT detectors as a possible solution to enable high operating temperatures. For this reason, we extended the simulation campaign to $T = 260\,\text{K}$.

It should be emphasized that detectors generally have anti-reflective coating (ARC) deposited on their illuminated face, which is very difficult to include in the simulation setup. To overcome this problem without sacrificing the inclusion of an ARC, we defined the illumination source reference plane just inside the substrate, as shown in Fig. 6(a). With this approach, not only a more realistic estimate of $\mathcal{R}$ can be achieved, but also the optical cavity effect (i.e., the OC resonance) is significantly reduced, as expected in fabricated devices including a well-designed ARC.

We have performed an electromagnetic FDTD simulation for each λ- and Λ-point as in Section 3, now followed by a simulation of the carrier transport problem, which yields the dark current, the photocurrent, the responsivity $\mathcal{R}$ and finally the spectral specific detectivity D^*. In the carrier transport simulation, the bias contact is defined at the pixel nanodisks, which are deposited on the n-doped, wide bandgap HgCdTe layer, and the ground contact is connected to the reflector as shown in Fig. 6(b) for the elementary cell. The electrical simulations have been performed by operating the detector in reverse bias to $V_{bias} = -0.5\,\text{V}$, in the dark and under illumination, for $\Lambda \in [0.3, 2.4]\,\mu\text{m}$, and in the waveband $\lambda \in [0.25, 5.5]\,\mu\text{m}$.

Figure 6(c) shows the obtained 2D color map of $\mathcal{R}$ at $T = 160\,\text{K}$, where we have also shown the fundamental SPP mode λ_{SPP} as a black slanted line. The "upper" and "lower" modes are clearly visible, and they arise from the interaction between the SPP mode λ_{SPP} and the OC mode at $\lambda_m \approx 5\,\mu\text{m}$, not shown in the figure.

To obtain more quantitative results, we compared the properties of the considered plasmonic detector with $t_{abs} = 0.8\,\mu\text{m}$ and $\Lambda = 1.3\,\mu\text{m}$, with a standard (i.e., non-plasmonic) one, whose absorber is identical except for the thickness, i.e., $t_{abs} = 5\,\mu\text{m}$. The two elementary cells are shown in Fig. 7(a), for which PBC along $\hat{x}$, $\hat{y}$ and CPML along $\hat{z}$ have been applied as usual. Figure 7(b) shows that the plasmonic detector is characterized by the lowest values of J_{dark} due to
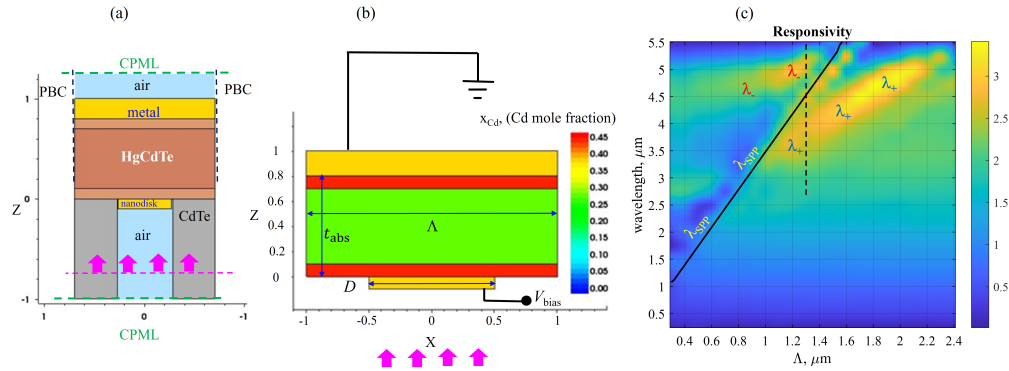
Fig. 6. (a) 2D cutplane showing the simulated elementary cell with $t_{abs} = 0.8$ μm, with PBC on the lateral domain boundaries and CPML on the upper and lower domain boundaries. The horizontal dashed line across the substrate represents the illuminating source plane. (b) Scheme of the electrical contacts. (c) Color map of the responsivity in the (Λ, λ) parameter space at $T = 160$ K. The "lower" and "upper" hybrid plasmon resonances calculated according to Eq. (13) are well visible and marked as λ_- and λ_+, respectively. The solid black oblique line is the λ_{SPP} mode, and the dashed vertical line marks $\Lambda = 1.3$ μm, as a reference for spectra plotted in Fig. 7.

the smaller thickness of the absorber and the difference with the thicker standard detector is more significant for the highest temperature.

Figure 7(c) shows that temperature has only a limited effect on responsivity, and the most notable effect of increasing T is a blue shift of the cut-off wavelength. Figure 7(d),(e) show the spectra of specific detectivity D^* for the plasmonic and for the standard detector, for $T = 160$ K and 260 K. Since the plasmonic detector is much thinner than the standard one, its dark current is lower by a factor of ≈ 3 at $T = 160$ K and by a factor of ≈ 4.6 at $T = 260$ K at the operating reverse bias. Since $\mathcal{R}$ for the plasmonic detector is only slightly penalized around the peak, the specific detectivity D^* increases significantly with respect to the thick standard detector for both temperature values, which was the primary goal for the pursued approach.

Apart from the enhancement of D^*, the other notable effect is the splitting of the D^* peak, which occurs only for the plasmonic detector (Fig. 7(d),(e), solid lines). This is caused by the SPP-OC interaction, which makes the plasmons to hybridize, as described in Section 3.3. The resulting "upper" and "lower" resonances (λ_+ and λ_-, respectively) are both visible at the lowest temperature (Fig. 7(d), solid line), and the net macroscopic effect on the detector performance is the broadening of the optical response, which is an important point as it leads to an increase in the usable waveband.

It is important to remark that the λ_- resonance at $T = 260$ K results beyond the cut-off wavelength, which means that, although it exists as a Hamiltonian eigenvalue, it is ineffective because it does not absorb at this temperature (in fact, in the D^* spectrum it is not visible). This indicates that the MCT bandgap must be always optimized for the desired operating temperature. For example, if the detector must operate up to $\lambda = 5.5$ μm at $T = 260$ K, the Cd mole fraction for the MCT absorber layer should be slightly reduced.

As a final consideration, it is pointed that the small decrease in responsivity for the plasmonic detector, which incidentally is limited around its peak value, can be avoided by considering plasmonic materials other than gold, e.g., indium-tin-oxide or heavily doped semiconductor layers [29,32,45,46], which avoid the backscattering of light hitting the nanodisks. This is one of the many improvements and optimizations that can be considered, but they are beyond the scope of this paper.
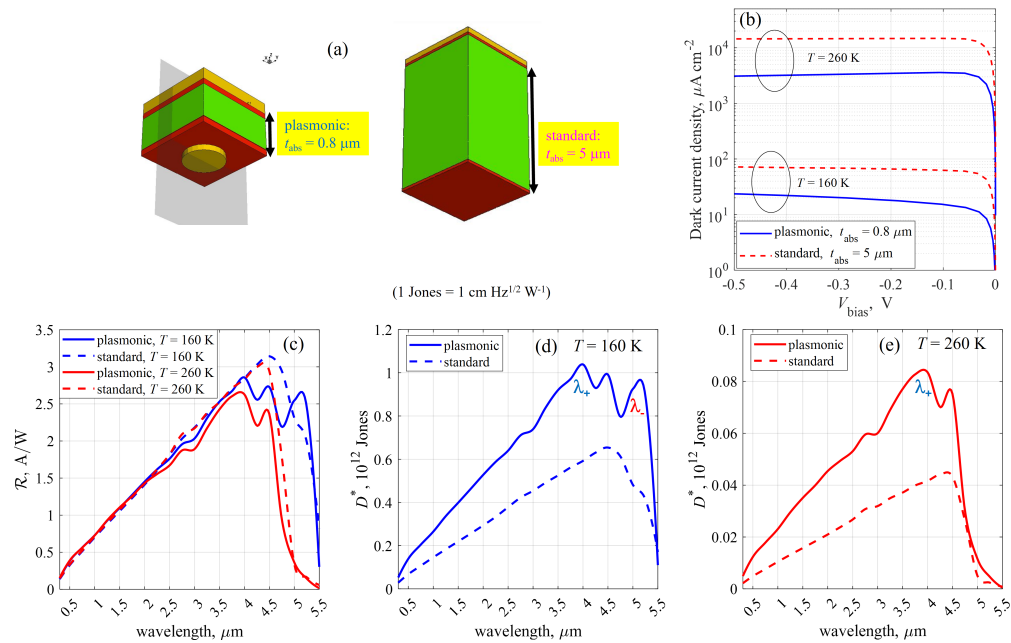
Fig. 7. (a) 3D scheme of the plasmonic, 0.8 μm-thick elementary cell and the corresponding standard 5 μm-thick detector with gold reflector. (b) Dark current density for the plasmonic and for the standard detector, for $T = 160\,\text{K}$ and $260\,\text{K}$, with in panel (c) the corresponding $\mathcal{R}$ spectra. D^* spectra for the plasmonic and for the standard detector, for (d) $T = 160\,\text{K}$ and for (e) $T = 260\,\text{K}$.

5. Conclusions

The motivation to consider plasmonic cavities with MCT is ultimately to use very thin absorbers without penalizing $\mathcal{R}$, which could lead to the fabrication of IR detectors with reduced dark current and improved D^*. The most relevant potential of such solution is to operate close to room temperature, i.e., to fabricate IR detectors without heavy and expensive cooling systems, exploiting, e.g., Peltier cells.

To show the possibilities afforded by a similar detector architecture, we have presented a detailed investigation of the absorption properties of a plasmonic IR photodetector for the MWIR band where an HgCdTe absorber is embedded in a plasmonic cavity. The absorber has been designed much thinner than that of usual devices (less than 1 μm) to reduce the dark current. The plasmonic resonances compensate for the reduction in absorption resulting from the use of a very thin absorber layer, with the net effect of achieving a responsivity which is only slightly lower than that of a standard detector with a thickness of 5 μm. The final result is a specific detectivity that exceeds the corresponding standard detector D^* by a factor of ≈ 2 around the spectral peak. These properties hold even at $T = 260$ K, a temperature that does not require heavy and expensive cooling systems, suggesting that plasmonics is a technology that can lead to HOT detectors, with the positive side effect to reduce the use of mercury-based materials, which are potentially hazardous.

However, there is a secondary positive impacts to be considered: the presence of the SPP-OC interactions that split the plasmonic mode into two hybrid modes, leading to the "upper" and "lower" hybrid resonances, which enable to broaden the optical spectral response ($\mathcal{R}$ and D^*), as described in Section 3.3, offering the chance to cover the entire MWIR band with a single detector.

Last advantage is that, when the detector is very thin, you can extract the carriers quickly since the carriers transit time depends on the absorber thickness [98]. This leads to higher frequency response, an important characteristic is many applications.

The next steps originated by this work could involve the use of different materials other than gold as plasmonic metal for MWIR, investigating the response to more complex excitation fields, taking into account the spatial finiteness, e.g., with Gaussian beams. This could enable to extend the modeling campaigns including other significant figures of merit, such as inter-pixel crosstalk. This could be the starting point towards further optimizations of the absorber and/or the nanodisk array, possibly considering alternative metals or conductive materials.

Supplemental document. See Supplement 1 for supporting content.

References

1. T. Ashley and C. T. Elliott, "Model for minority carrier lifetimes in doped HgCdTe," Electron. Lett. **21**(10), 451–452 (1985).
2. C. T. Elliott, "Non-equilibrium modes of operation of narrow-gap semiconductor devices," Semicond. Sci. Technol. **5**(3S), S30–S37 (1990).
3. P. Martyniuk and A. Rogalski, "HOT infrared photodetectors," Opto-Electron. Rev. **21**(2), 239–257 (2013).
4. S. Maimon and G. W. Wicks, "*nBn* detector, an infrared detector with reduced dark current and higher operating temperature," Appl. Phys. Lett. **89**(15), 151109 (2006).
5. A. M. Itsuno, J. D. Phillips, and S. Velicu, "Predicted performance improvement of Auger-suppressed HgCdTe photodiodes and *p-n* heterojunction detectors," IEEE Trans. Electron Devices **58**(2), 501–507 (2011).
6. A. M. Itsuno, J. D. Phillips, and S. Velicu, "Mid-wave infrared HgCdTe nBn photodetector," Appl. Phys. Lett. **100**(16), 161102 (2012).
7. J. He, P. Wang, Q. Li, *et al.*, "Enhanced performance of HgCdTe long-wavelength infrared photodetectors with nBn design," IEEE Trans. Electron Devices **67**(5), 2001–2007 (2020).
8. I. D. Burlakov, N. A. Kulchitsky, A. V. Voitsekhovskii, *et al.*, "Unipolar semiconductor barrier structures for infrared photodetector arrays (review)," J. Commun. Technol. Electron. **66**(9), 1084–1091 (2021).
9. A. V. Voitsekhovskii, S. M. Dzyadukh, D. I. Gorn, *et al.*, "Comprehensive experimental study of NBνN barrier structures based on n-HgCdTe MBE for detection in MWIR and LWIR spectra," Phys. Scr. **98**(6), 065907 (2023).
10. M. Vallone, M. G. C. Alasio, A. Tibaldi, *et al.*, "Exploring optimal dark current design in HgCdTe infrared barrier detectors: a TCAD and semianalytic investigation," IEEE Photonics J. **16**(1), 1–8 (2024).
11. R. Sellers, S. Sonde, P. Man, *et al.*, "Fabrication and modeling study to reduce valence band offset in HgCdTe MWIR nBn photodetectors grown on silicon using superlattice barriers," Proc. SPIE **PC12687** PC1268709 (2023).
12. W. Lei, J. Antoszewski, and L. Faraone, "Progress, challenges, and opportunities for HgCdTe infrared materials and detectors," Appl. Phys. Rev. **2**(4), 041303 (2015).
13. J. Schuster, W. E. Tennant, E. Bellotti, *et al.*, "Analysis of the Auger recombination rate in $P^+N-n-N-N$ HgCdTe detectors for HOT applications," Proc. SPIE **9819** 98191F (2016).
14. D. Lee, M. Carmody, E. Piquette, *et al.*, "High-operating temperature HgCdTe: A vision for the near future," J. Electron. Mater. **45**(9), 4587–4595 (2016).
15. J. Schuster, R. E. DeWames, and P. S. Wijewarnasurya, "Dark currents in a fully-depleted LWIR HgCdTe *P*-on-*n* heterojunction: analytical and numerical simulations," J. Electron. Mater. **46**(11), 6295–6305 (2017).
16. D. Lee, P. Dreiske, J. Ellsworth, *et al.*, "Law 19: The ultimate photodiode performance metric," Proc. SPIE **11407** 114070X (2020).
17. A. Rogalski, P. Martyniuk, M. Kopytko, *et al.*, "Trends in performance limits of the HOT infrared photodetectors," Appl. Sci. **11**(2), 501 (2021).
18. P. Martyniuk, M. Kopytko, and A. Rogalski, "Barrier infrared detectors," Opto-Electron. Rev. **22**(2), 127–146 (2014).

19. P. Madejczyk, W. Gawron, J. Sobieski, *et al.*, "MCT heterostructures for higher operating temperature infrared detectors designed in Poland," Opto-Electron. Rev. **31**, e144551 (2023).
20. A. Tibaldi, J. A. Gonzalez Montoya, M. Vallone, *et al.*, "Modeling infrared superlattice photodetectors: From nonequilibrium Green's functions to quantum-corrected drift diffusion," Phys. Rev. Appl. **16**(4), 044024 (2021).
21. A. Rogalski, *Infrared Detectors* (CRC Press, 2011), 2nd ed.
22. J. G. A. Wehner, E. P. G. Smith, G. M. Venzor, *et al.*, "HgCdTe photon trapping structure for broadband mid-wavelength infrared absorption," J. Electron. Mater. **40**(8), 1840–1846 (2011).
23. J. Schuster and E. Bellotti, "Analysis of optical and electrical crosstalk in small pitch photon trapping HgCdTe pixel arrays," Appl. Phys. Lett. **101**(26), 261118 (2012).
24. J. Rosenberg, R. V. Shenoi, S. Krishna, *et al.*, "Design of plasmonic photonic crystal resonant cavities for polarization sensitive infrared photodetectors," Opt. Express **18**(4), 3672–3686 (2010).
25. S. Q. Li, P. Guo, L. Zhang, *et al.*, "Infrared plasmonics with indium-tin-oxide nanorod arrays," ACS Nano **5**(11), 9161–9170 (2011).
26. A. Agrawal, I. Kriegel, and D. J. Milliron, "Shape-dependent field enhancement and plasmon resonance of oxide nanocrystals," J. Phys. Chem. C **119**(11), 6227–6238 (2011).
27. J. Tong, L. Y. M. Tobing, S. Qiu, *et al.*, "Room temperature plasmon-enhanced InAs$_{0.91}$Sb$_{0.09}$-based heterojunction *n-i-p* mid-wave infrared photodetector," Appl. Phys. Lett. **113**(1), 011110 (2018).
28. K. Tappura, "Enhancing the performance of commercial infrared detectors by surface plasmons," Eurosensors **2**, 1063 (2018).
29. N. Vanamala, K. C. Santiago, and N. C. Das, "Enhanced MWIR absorption of HgCdTe (MCT) via plasmonic metal oxide nanostructures," AIP Adv. **9**(2), 025113 (2019).
30. N. Vanamala, K. C. Santiago, N. C. Das, *et al.*, "Geometric optimization of plasmonic nanostructure arrays on MWIR HgCdTe (MCT)," AIP Adv. **10**(6), 065006 (2020).
31. J. Budhu, N. Pfiester, K.-K. Choi, *et al.*, "Dielectric resonator antenna coupled antimonide-based detectors (DRACAD) for the infrared," IEEE Trans. Antennas Propagat. **69**(10), 6762–6771 (2021).
32. G. Zhang, C. Xu, D. Sun, *et al.*, "Metasurface-tuned light-matter interactions for high-performance photodetectors," Fundam. Res. (in press) (2024).
33. H. Raether, *Surface Plasmons on Smooth and Rough Surfaces and on Gratings*, vol. 111 of Springer Tracts in Modern Physics (Springer-Verlag, 1988).
34. Z. Han and S. I. Bozhevolnyi, "Radiation guiding with surface plasmon polaritons," Rep. Prog. Phys. **76**(1), 016402 (2013).
35. W. D. Lawson, S. Nielsen, E. H. Putley, *et al.*, "Preparation and properties of HgTe and mixed crystals of HgTe-CdTe," J. Phys. Chem. Solids **9**(3-4), 325–329 (1959).
36. M. A. Kinch, "The future of infrared; III-Vs or HgCdTe?" J. Electron. Mater. **44**(9), 2969–2976 (2015).
37. P. Wang, H. Xia, Q. Li, *et al.*, "Sensing infrared photons at room temperature: from bulk materials to atomic layers," Small **15**(46), 1904396 (2019).
38. M. Kopytko and A. Rogalski, "Performance evaluation of type-II superlattice devices relative to HgCdTe photodiodes," IEEE Trans. Electron Devices **69**(6), 2992–3002 (2022).
39. M. A. Kinch, F. Aqariden, D. Chandra, *et al.*, "Minority carrier lifetime in *p*-HgCdTe," J. Electron. Mater. **34**(6), 880–884 (2005).
40. L. Ciura, M. Kopytko, and P. Martyniuk, "Low-frequency noise limitations of InAsSb-, and HgCdTe-based infrared detectors," Sens. Actuators, A **305**, 111908 (2020).
41. F. Bonani and G. Ghione, *Noise in Semiconductor Devices. Modeling and Simulation*, Advanced Microelectronics (Springer-Verlag, 2001).
42. V. G. Kravets, A. V. Kabashin, W. L. Barnes, *et al.*, "Plasmonic surface lattice resonances: A review of properties and applications," Chem. Rev. **118**(12), 5912–5951 (2018).
43. M. Vallone, A. Tibaldi, S. Hanna, *et al.*, "Plasmon-enhanced light absorption in mid-wavelength infrared HgCdTe detectors," IEEE J. Select. Topics Quantum Electron. **28**(2: Optical Detectors), 1–10 (2022).
44. Z. Wang, L. Li, S. Wei, *et al.*, "Manipulating light-matter interaction into strong coupling regime for photon entanglement in plasmonic lattices," J. Appl. Phys. **133**(6), 063101 (2023).
45. L. Nordin, P. Petluru, A. Kamboj, *et al.*, "Ultra-thin plasmonic detectors," Optica **8**(12), 1545–1551 (2021).
46. N. Yan, Y. Qiu, X. He, *et al.*, "Plasmonic enhanced nanocrystal infrared photodetectors," Mater. **16**, 3216 (2023).
47. M. D. Goldflam, E. A. Kadlec, B. V. Olson, *et al.*, "Enhanced infrared detectors using resonant structures combined with thin type-II superlattice absorbers," Appl. Phys. Lett. **109**(25), 251103 (2016).
48. Y. Todorov, L. Tosetto, J. Teissier, *et al.*, "Optical properties of metal-dielectric-metal microcavities in the thz frequency range," Opt. Express **18**(13), 13886–13907 (2010).
49. L. Liu, Y. Chen, Z. Huang, *et al.*, "Highly efficient metallic optical incouplers for quantum well infrared photodetectors," Sci. Rep. **6**(1), 30414 (2016).
50. P.-B. Vigneron, S. Pirotta, I. Carusotto, *et al.*, "Quantum well infrared photo-detectors operating in the strong light-matter coupling regime," Appl. Phys. Lett. **114**(13), 131104 (2019).
51. C. R. Gubbin, S. D. Liberato, and T. G. Folland, "Surface phonon polaritons for infrared optoelectronics," J. Appl. Phys. **131**(3), 030901 (2022).

52. C. Haffner, W. Heni, Y. Fedoryshyn, *et al.*, "All-plasmonic Mach–Zehnder modulator enabling optical high-speed communication at the microscale," Nature Photon. **9**(8), 525–528 (2015).

53. C. Haffner, W. Heni, Y. Fedoryshyn, *et al.*, "Plasmonic organic hybrid modulators–scaling highest speed photonics to the microscale," Proc. IEEE **104**(12), 2362–2379 (2016).

54. A. Tibaldi, M. Ghomashi, F. Bertazzi, *et al.*, "Plasmonic-organic hybrid electro/optic Mach-Zehnder modulators: from waveguide to multiphysics modal-FDTD modeling," Opt. Express **28**(20), 29253–29271 (2020).

55. J. Zhou, J. Deng, M. Shi, *et al.*, "Cavity coupled plasmonic resonator enhanced infrared detectors," Appl. Phys. Lett. **119**(16), 160504 (2021).

56. J.-M. Manceau, G. Biasiol, N. L. tran, *et al.*, "Immunity of intersubband polaritons to inhomogeneous broadening," Phys. Rev. B **96**(23), 235301 (2017).

57. C. Hägglund, G. Zeltzer, R. Ruiz, *et al.*, "Strong coupling of plasmon and nanocavity modes for dual-band, near-perfect absorbers and ultrathin photovoltaics," ACS Photon. **3**(3), 456–463 (2016).

58. Z. Zhou, M. Sang, J. Zhang, *et al.*, "Narrowband HgCdTe infrared photodetector with integrated plasmonic structure," Opt. Lett. **48**(7), 1882–1885 (2023).

59. J. Su, C. Li, J. Xiao, *et al.*, "Boosting infrared absorption through surface plasmon resonance enhanced HgCdTe microcavity," J. Appl. Phys. **134**(24), 243106 (2023).

60. H. Ge, R. Xie, Y. Chen, *et al.*, "Skin effect photon-trapping enhancement in infrared photodiodes," Opt. Express **29**(15), 22823–22837 (2021).

61. W. E. Tennant, D. Lee, M. Zandian, *et al.*, "MBE HgCdTe technology: A very general solution to IR detection, described by "Rule 07", a very convenient heuristic," J. Electron. Mater. **37**(9), 1406–1410 (2008).

62. M. Vallone, M. Goano, F. Bertazzi, *et al.*, "Reducing inter-pixel crosstalk in HgCdTe detectors," Opt. Quantum Electron. **52**(1), 25 (2020).

63. M. Vallone, M. Goano, F. Bertazzi, *et al.*, "Comparing FDTD and ray tracing models in the numerical simulation of HgCdTe LWIR photodetectors," J. Electron. Mater. **45**(9), 4524–4531 (2016).

64. M. Vallone, M. Goano, F. Bertazzi, *et al.*, "Simulation of small-pitch HgCdTe photodetectors," J. Electron. Mater. **46**(9), 5458–5470 (2017).

65. M. Vallone, M. Goano, A. Tibaldi, *et al.*, "Quantum efficiency and crosstalk in subwavelength HgCdTe dual band infrared detectors," IEEE J. Select. Topics Quantum Electron. **28**(2: Optical Detectors), 3800309 (2022).

66. Synopsys, Inc., Optical Solutions Group, Ossining, NY, *RSoft FullWAVE User Guide, v2019.09* (2019).

67. J.-P. Berenger, "A perfectly matched layer for the absorption of electromagnetic waves," J. Comp. Phys. **114**(2), 185–200 (1994).

68. M. Vallone, M. Goano, F. Bertazzi, *et al.*, "FDTD simulation of compositionally graded HgCdTe photodetectors," Infrared Phys. Technol. **97**, 203–209 (2019).

69. Synopsys, Inc., Mountain View, CA, *Sentaurus Device User Guide. Version N-2017.09* (2017).

70. J. D. Jackson, *Classical Electrodynamics* (Wiley, 1999), 3rd ed.

71. M. Born and E. Wolf, *Principles of Optics. Electromagnetic Theory of Propagation, Interference and Diffraction of Light* (Cambridge University Press, 1999), 7th ed.

72. S. J. Orfanidis, "Electromagnetic waves and antennas," https://www.ece.rutgers.edu/orfanidi/ewa/ (2016).

73. C. Keasler and E. Bellotti, "Three-dimensional electromagnetic and electrical simulation of HgCdTe pixel arrays," J. Electron. Mater. **40**(8), 1795–1801 (2011).

74. J. Liang, W. Hu, Z. Ye, *et al.*, "Improved performance of HgCdTe infrared detector focal plane arrays by modulating light field based on photonic crystal structure," J. Appl. Phys. **115**(18), 184504 (2014).

75. C. A. Hougen, "Model for infrared absorption and transmission of liquid-phase epitaxy $Hg_{1-x}Cd_xTe$," J. Appl. Phys. **66**(8), 3763–3766 (1989).

76. P. Capper and J. Garland, eds. *Mercury Cadmium Telluride. Growth, Properties and Applications* (John Wiley & Sons, 2011).

77. M. A. Ordal, L. L. Long, R. J. Bell, *et al.*, "Optical properties of the metals Al, Co, Cu, Au, Fe, Pb, Ni, Pd, Pt, Ag, Ti, and W in the infrared and far infrared," Appl. Opt. **22**(7), 1099–1119 (1983).

78. D. Vasileska, S. M. Goodnick, and G. Klimeck, *Computational Electronics. Semiclassical and Quantum Device Modeling and Simulation* (CRC Press, 2010).

79. M. Goano, F. Bertazzi, X. Zhou, *et al.*, "Challenges towards the simulation of GaN-based LEDs beyond the semiclassical framework," Proc. SPIE **9742** 974202 (2016).

80. M. Vallone, M. Mandurrino, M. Goano, *et al.*, "Numerical modeling of SRH and tunneling mechanisms in high-operating-temperature MWIR HgCdTe photodetectors," J. Electron. Mater. **44**(9), 3056–3063 (2015).

81. V. C. Lopes, A. J. Syllaios, and M. C. Chen, "Minority carrier lifetime in mercury cadmium telluride," Semiconductor Sci. Technol. **8**(6S), 824–841 (1993).

82. A. Yariv and P. Yeh, *Photonics: Optical Electronics and Modern Communications* (Oxford University Press, 2007), 6th ed.

83. Z. Han, E. Forsberg, and S. He, "Surface plasmon Bragg gratings formed in metal-insulator-metal waveguides," IEEE Photonics Technol. Lett. **19**(2), 91–93 (2007).

84. L. A. Coldren, S. W. Corzine, and M. L. Masanovic, *Diode Lasers and Photonic Integrated Circuits* (John Wiley & Sons, 2012), 2nd ed.

85. M. E. Peskin and D. V. Schroeder, *Quantum Field Theory* (CRC Press, 1995).

86. F. Mandl and B. Shaw, *Quantum Field Theory, 2nd Edition* (Wiley, 2010).
87. C. Ciuti, G. Bastard, and I. Carusotto, "Quantum vacuum properties of the intersubband cavity polariton field," Phys. Rev. B **72**(11), 115303 (2005).
88. Y. Todorov and C. Sirtori, "Intersubband polaritons in the electrical dipole gauge," Phys. Rev. B **85**(4), 045304 (2012).
89. A. Vasanelli, Y. Todorov, and C. Sirtori, "Ultra-strong light–matter coupling and superradiance using dense electron gases," C. R. Phys. **17**(8), 861–873 (2016).
90. D. G. Baranov, B. Munkhbat, E. Zhukova, *et al.*, "Ultrastrong coupling between nanoparticle plasmons and cavity photons at ambient conditions," Nature Commun. **11**(1), 2715 (2020).
91. N. S. Mueller, Y. Okamura, B. G. M. Vieira, *et al.*, "Deep strong light–matter coupling in plasmonic nanoparticle crystals," Nature **583**(7818), 780–784 (2020).
92. R. H. Dicke, "Coherence in spontaneous radiation processes," Phys. Rev. **93**(1), 99–110 (1954).
93. J. J. Hopfield, "Theory of the contribution of excitons to the complex delectric constant of crystals," Phys. Rev. **112**(5), 1555–1567 (1958).
94. H. A. Haus and W. Huang, "Coupled-mode theory," Proc. IEEE **79**(10), 1505–1518 (1991).
95. J. Raab, F. P. Mezzapesa, L. Viti, *et al.*, "Ultrafast terahertz saturable absorbers using tailored intersubband polaritons," Nature Commun. **11**(1), 4290 (2022).
96. A. F. Kockum, A. Miranowicz, S. D. Liberato, *et al.*, "Ultrastrong coupling between light and matter," Nature Rev. Phys. **1**(1), 19–40 (2019).
97. F. Pisani, D. Gacemi, A. Vasanelli, *et al.*, "Electronic transport driven by collective light-matter coupled states in a quantum device," Nature Commun. **14**(1), 3914 (2023).
98. M. G. C. Alasio, M. Vallone, A. Tibaldi, *et al.*, "TCAD-assisted progress on the Cisco platform towards low-bias 200 Gbit/s vertical-*pin* Ge-on-Si waveguide photodetectors," J. Lightwave Technol. **42**(9), 3269–3276 (2024).